

bility of some relaxation process unique to quantum Hall ferromagnets cannot be ruled out at this time.

In particular, coupling to nuclear spins may be responsible for the origin of the slow relaxation in the vicinity of the  $\nu = 2/5$  FQHE. In GaAs, the lattice nuclei consist of  $S = 3/2$  nuclear isotopes of  $^{69}\text{Ga}$  and  $^{71}\text{Ga}$  and  $^{75}\text{As}$  with which conduction electrons interact through hyperfine coupling. In general, the coupling between electronic and nuclear spins is extremely weak and the relaxations of nuclear spins occur at a negligibly slow rate. However, presence of low-energy spin excitations has been shown to enhance the coupling between the spins of electrons and nuclei in the quantum Hall regime. At  $\nu = 1$ , presence of electron spin texture excitation known as Skyrmions (*1, 6*) leads to an enhanced nuclear spin diffusion and gives rise to a large heat capacity at low temperatures (*19, 20*). An earlier experiment also has shown that nuclear spin polarization can produce hysteresis and memory effects in the magnetotransport (*35*). Consequently, enhanced coupling to nuclear spins cannot be ruled out in our experiment. A possible route of coupling between nuclear and electronic spins is through existence of a Skyrmion-like excitation associated with the  $\nu = 1/3$  FQHE state. Because the  $\nu = 2/5$  FQHE state can be considered to be a daughter state of the  $\nu = 1/3$  state, Skyrmionic excitations from the  $\nu = 1/3$  FQHE state may be responsible for the coupling to the nuclear spin in the  $\nu = 2/5$ . Alternatively, the quasiparticles from the  $\nu = 1/3$  FQHE that nucleate the  $\nu = 2/5$  FQHE couple to the nuclear spins may be giving rise to the observed slow dynamics. Further experiments will be necessary to elucidate the coupling to nuclear spin in the FQHE regime.

In conclusion, we have observed transport and relaxational behavior associated with the ferromagnetic ordering in the FQHE regime of a 2DES. Our experiment demonstrates a previously unknown type of magnetic ordering of FQHE states and a slow, aging effect associated with multidomain structure. Further experiments should reveal additional properties of this many-body magnetism. In particular, we speculate on the nature of quantum Hall magnetism at micrometer or sub-micrometer lengthscales. Study of single domain dynamics in the quantum Hall ferromagnets should reveal time-dependent phenomena such as macroscopic quantum tunneling, switching, and telegraphic behaviors. Detection of such effects should lead to greater understanding of many-body magnetism and quantum mechanics at small lengthscales.

References and Notes

1. S. Das Sarma and A. Pinczuk, Eds., *Perspectives on Quantum Hall Effects* (Wiley, New York, 1997).  
 2. R. E. Prange and S. M. Girvin, Eds., *The Quantum Hall Effect* (Springer-Verlag, New York, 1990).

3. S. L. Sondhi, S. M. Girvin, J. P. Carini, D. Shahar, *Rev. Mod. Phys.* **69**, 315 (1997).  
 4. H. P. Wei, D. C. Tsui, A. M. M. P. Pruisken, *Phys. Rev. B* **33**, 1488 (1986).  
 5. H. P. Wei, D. C. Tsui, M. A. Paalanen, A. M. M. P. Pruisken, *Phys. Rev. Lett.* **61**, 1294 (1988).  
 6. S. M. Girvin and A. H. MacDonald, in (*1*), pp. 161–224.  
 7. T. Jungwirth, S. Shukla, L. Smrcka, M. Shayegan, A. H. MacDonald, *Phys. Rev. Lett.* **81**, 2328 (1998).  
 8. A. H. MacDonald, R. Rajaraman, T. Jungwirth, *Phys. Rev. B* **60**, 8817 (1999).  
 9. S. Q. Murphy, J. P. Eisenstein, G. S. Boebinger, L. N. Pfeiffer, K. W. West, *Phys. Rev. Lett.* **72**, 728 (1994).  
 10. K. Yang et al., *Phys. Rev. Lett.* **72**, 732 (1994).  
 11. A. Sawada et al., *Phys. Rev. Lett.* **80**, 4534 (1998).  
 12. V. Piazza et al., *Nature* **402**, 638 (1999).  
 13. J. P. Eisenstein, H. L. Stormer, L. N. Pfeiffer, K. W. West, *Phys. Rev. Lett.* **62**, 1540 (1989).  
 14. R. G. Clark et al., *Phys. Rev. Lett.* **62**, 1536 (1989).  
 15. J. P. Eisenstein, H. L. Stormer, L. N. Pfeiffer, K. W. West, *Phys. Rev. B* **41**, 7910 (1990).  
 16. L. W. Engel, S. W. Hwang, T. Sajoto, D. C. Tsui, M. Shayegan, *Phys. Rev. B* **45**, 3418 (1992).  
 17. R. R. Du et al., *Phys. Rev. Lett.* **75**, 3926 (1995).  
 18. H. Cho et al., *Phys. Rev. Lett.* **81**, 2522 (1998).  
 19. V. Bayot, E. Grivei, J. M. Beuken, S. Melinte, M. Shayegan, *Phys. Rev. Lett.* **79**, 1718 (1997).  
 20. S. Melinte, E. Grivei, V. Bayot, M. Shayegan, *Phys. Rev. Lett.* **82**, 2764 (1999).  
 21. S. A. J. Wieggers et al., *Phys. Rev. Lett.* **79**, 3228 (1997).  
 22. J. J. Prejean and J. Souletie, *J. Phys. (Paris)* **41**, 1335 (1980).  
 23. D. K. Lottis, R. M. White, E. D. Dahlberg, *Phys. Rev. Lett.* **67**, 362 (1991).  
 24. W. F. Brown, *Phys. Rev.* **130**, 1677 (1963).  
 25. E. M. Chudnovsky and L. Gunther, *Phys. Rev. Lett.* **60**, 661 (1988).  
 26. M. Enz and R. Schilling, *J. Phys. C* **19**, 1765 (1986).  
 27. J. L. van Hemmen and A. Suto, *Europhys. Lett.* **1** 481 (1986).  
 28. L. Gunther and B. Barbara, Eds., *Quantum Tunneling of the Magnetization* (North American Treaty Organization Advanced Study Institute, Kluwer, Dordrecht, Netherlands, 1995), series E, vol. 301.  
 29. E. Vincent, J. Hammann, M. Ocio, J. P. Bouchaud, L. F. Cugliandolo, in *Complex Behaviour of Glassy Systems: Proceedings of the XIV Sitges Conference*, Sitges, Spain, M. Rubi and C. Perez-Vicente, Eds. (Springer-Verlag, Berlin, 1997), pp. 184–219 and references therein.  
 30. H. Yamazaki, G. Tatara, K. Katsumata, K. Ishibashi, Y. Aoyagi, *J. Magn. Magn. Mater.* **156**, 135 (1996).  
 31. J. E. Wegrowe et al., *Phys. Rev. B* **52**, 3466 (1995).  
 32. J. E. Wegrowe et al., *Europhys. Lett.* **38**, 329 (1997).  
 33. F. Alberici-Kious, J. P. Bouchaud, L. F. Cugliandolo, P. Doussineau, A. Levelut, *Phys. Rev. Lett.* **81**, 4987 (1998).  
 34. J. Eom et al., unpublished data.  
 35. M. Dohers, K. v. Klitzing, J. Schneider, G. Weimann, K. Ploog, *Phys. Rev. Lett.* **61**, 1650 (1988).  
 36. We thank A. MacDonald and G. Mazenko for useful discussions. The work at the University of Chicago was supported in part by the Material Research Science and Engineering Center Program of the National Science Foundation (grant no. DMR-9808595) and the David and Lucille Packard Foundation.

28 April 2000; accepted 23 August 2000

# Imaging Coherent Electron Flow from a Quantum Point Contact

M. A. Topinka,<sup>1</sup> B. J. LeRoy,<sup>1</sup> S. E. J. Shaw,<sup>1</sup> E. J. Heller,<sup>1</sup> R. M. Westervelt,<sup>1\*</sup> K. D. Maranowski,<sup>2</sup> A. C. Gossard<sup>2</sup>

Scanning a charged tip above the two-dimensional electron gas inside a gallium arsenide/aluminum gallium arsenide nanostructure allows the coherent electron flow from the lowest quantized modes of a quantum point contact at liquid helium temperatures to be imaged. As the width of the quantum point contact is increased, its electrical conductance increases in quantized steps of  $2e^2/h$ , where  $e$  is the electron charge and  $h$  is Planck's constant. The angular dependence of the electron flow on each step agrees with theory, and fringes separated by half the electron wavelength are observed. Placing the tip so that it interrupts the flow from particular modes of the quantum point contact causes a reduction in the conductance of those particular conduction channels below  $2e^2/h$  without affecting other channels.

The use of scanned probe microscopes (SPMs) in the study of mesoscopic physics has grown rapidly and has allowed direct imaging of a wide range of phenomena, including quantum corrals (*1–3*), electron flow through nanostructures (*4, 5*), charge distribution and photoactivity of dopant atoms (*6*), quantum Hall-effect edge states and liquids

(*7–9*), and spectra of metallic nanoclusters (*10*). Quantum point contacts (QPCs) formed in two-dimensional electron gases (2DEGs) have attracted strong attention. After the initial discovery that they show conductance quantization (*11, 12*), QPCs have been used in a wide variety of investigations, including transport through quantum dots, the quantum Hall effect, magnetic focusing, and the Aharonov-Bohm effect (*13*). Electron flow from QPCs has been studied both theoretically and experimentally (*14–15*). Although the basic concepts are understood, many interesting issues remain. Because they play such an important role in the operation of mesoscopic devices, QPCs make an

<sup>1</sup>Division of Engineering and Applied Sciences, Department of Physics, and Department of Chemistry and Chemical Biology, Harvard University, Cambridge, MA 02138, USA. <sup>2</sup>Materials Department, University of California, Santa Barbara, CA 93106, USA.

\*To whom correspondence should be addressed. E-mail: westervelt@deas.harvard.edu

ideal system to study with SPM techniques.

We present direct spatial images showing coherent electron flow from a QPC. The QPC was formed in the 2DEG below the surface of a GaAs/AlGaAs heterostructure, and images were obtained with the use of a capacitively coupled SPM tip (16). Mesoscopic structures offer approaches to novel electronics ranging from spintronics to quantum computers (17). Images of electron wave propagation that are sensitive to phase are needed to understand the fundamentals of electron motion and interaction in semiconductor nanostructures.

In the experimental technique used to image electron flow inside heterostructures (Fig. 1A), the sample is mounted in an atomic force microscope (AFM) and cooled to 1.7 K. The QPC is defined in the 2DEG inside a GaAs/AlGaAs heterostructure by two gates on the surface: applying a negative potential between the gates and the 2DEG forms a variable width channel. The conductance of the QPC is measured between two ohmic contacts. Electron flow from the QPC is imaged by scanning a negatively charged AFM tip above the surface of the device and simultaneously measuring the position-dependent conductance. Capacitive coupling reduces the density of the 2DEG in a small spot directly

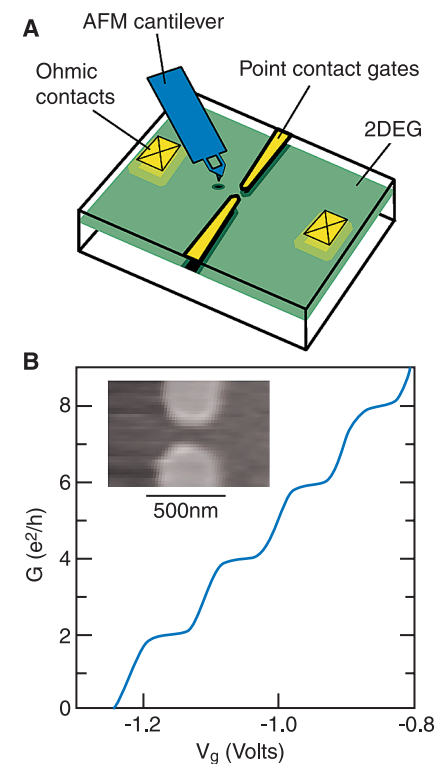


**Fig. 1.** (A) Schematic diagram of the experimental setup. QPC conductance is measured as a function of AFM tip position. (B) Point contact conductance  $G$  versus gate voltage  $V_g$  with no tip present at temperature  $T = 1.7$  K. Plateaus at integer multiples of  $2 e^2/h$  are clearly seen. The inset shows a topographic image of the point contact device.

beneath the tip, creating a depletion region that backscatters electron waves (Fig. 1A). When the tip is over areas of high electron flow, the conductance through the QPC is decreased; whereas when the tip is over areas of relatively low electron flow, the conductance through the QPC is unmodified. By

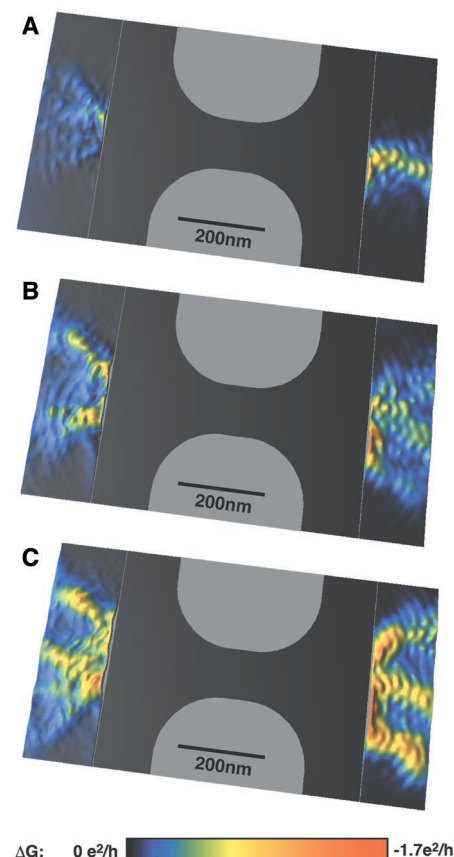


**Fig. 2.** Images of electron flow from a QPC of three increasing widths corresponding to (A) the first conductance plateau, (B) the second plateau, and (C) the third plateau. The color scale and the height in the third dimension show the change  $\Delta G$  in QPC conductance as the tip is scanned above the device. The gray areas outline the position of electrostatic gates.

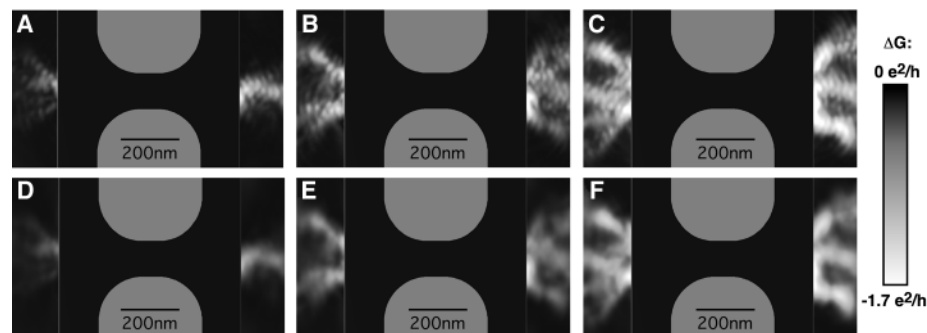


**Fig. 3.** Effect of electron heating on images of flow. (A) to (C) show electron flow for the first, second, and third conductance plateaus taken under the same conditions as in Fig. 2, A to C, with low voltage (0.2 mV) across the QPC. (D) to (F) show corresponding images for high voltage (3 mV) across the QPC, which causes electron heating. Heating destroys interference fringes but leaves the angular pattern unchanged.

scanning the tip over the sample, a 2D image of electron flow can be obtained. Because the tip is capacitively coupled to the 2DEG, no current flows between the tip and the 2DEG. Because the tip is elevated above the surface of the heterostructure, the material is not strained, avoiding possible additional forces on electrons.

The heterostructure used in this experiment was grown by molecular beam epitaxy (MBE) on an n-type GaAs substrate. In growth order, the layers were: 1.0  $\mu\text{m}$  of GaAs, 22 nm of  $\text{Al}_{0.3}\text{Ga}_{0.7}\text{As}$ , a  $\delta$ -doped Si ( $8 \times 10^{12}/\text{cm}^2$ ) donor layer, and 30 nm of  $\text{Al}_{0.3}\text{Ga}_{0.7}\text{As}$ , ending with a 5-nm GaAs cap. The 2DEG resides 57 nm below the surface, with mobility  $\mu = 1.0 \times 10^6 \text{ cm}^2 \text{ V}^{-1} \text{ s}^{-1}$  and density  $n = 4.5 \times 10^{11}/\text{cm}^2$ . These values of mobility and density correspond to a mean free path  $\lambda = 11 \mu\text{m}$ , Fermi wavelength  $\lambda_F = 37 \text{ nm}$ , and Fermi energy  $E_F = 16 \text{ meV}$ . Electrical measurements of conductance were made with a lock-in amplifier at 11 kHz in a voltage-biased configuration. The root mean square (rms) voltage across the QPC was chosen to be either 0.2 or 3.0 mV. The AFM tip was held at  $-3.0 \text{ V}$  relative to the 2DEG, and the tip was scanned 13 nm above the surface of the heterostructure. As the width of the channel was increased by changing the gate voltage  $V_g$ , the conductance of the point contact showed well-defined conductance plateaus (Fig. 1B) at integer multiples of the conductance quantum  $2 e^2/h$ . The inset is an AFM image of the QPC gates taken after completing all electrical measurements.

Images of electron flow from the QPC as its width was opened from the first mode [QPC conductance ( $G$ ) =  $2 e^2/h$ ] through the second ( $G = 4 e^2/h$ ) and third ( $G = 6 e^2/h$ ) modes are shown (Fig. 2), where each image is composed of two separate scans: one to the left of the point contact and one to the right. One clear feature is the changing and widening angular structure of electron flow as the QPC channel becomes wider. As each new

## REPORTS

mode is opened in the QPC, new angular lobes of electron flow appear, and the flow pattern widens. The flow patterns do not change substantially along conductance plateaus; transitions occur only at rises between plateaus (Fig. 1B). The current flow pattern on both sides of the QPC is independent of the current direction.

Another feature of the images in Fig. 2 is the appearance of fringes spaced by half the Fermi wavelength  $\lambda_F/2$  transverse to the electron flow (18). These fringes are due to the alternating constructive and destructive interference of electrons backscattered from the tip, and they demonstrate that we are imaging coherent electron wave flow. Images of fringes and flow were obtained only for tip voltages sufficient to deplete the electron gas in a small spot directly underneath the tip. Coherent backscattering between the tip and the QPC forms a resonant path: The conductance oscillates once each time the path length increases by  $\lambda_F/2$ . By comparing the typical round-trip time for an electron traveling between the QPC and the tip ( $t_{\text{trip}} = d_{\text{trip}}/v_F = 2.5$  ps) with the phase coherence time (19)  $\tau_{\phi} = 64$  ps and the thermal time  $\tau_{\text{th}} = \pi\hbar/k_B T = 14$  ps (where  $k_B T$  is the Boltzmann constant times temperature), we confirm that neither decoherence (from  $\tau_{\phi}$ ) nor thermal smearing (from  $\tau_{\text{th}}$ ) should affect the appearance of these fringes. In these scans, the voltage across the point contact (0.2 mV) (which is  $\sim k_B T/e$ ) was not observed to cause thermal blurring, as confirmed by comparison of 0.2-mV images with 0.1-mV and 0.5-mV images. Another feature of these fringes is that their average amplitude, between 0.15 and  $0.25 e^2/h$  in all scans, changes little as the QPC conductance increases from  $G = 2 e^2/h$  to  $G = 16 e^2/h$ .

The consequences of using effectively hotter electrons to measure electron flow are shown (Fig. 3). The top three images (Fig. 3, A to C) were taken at low voltage (0.2 mV) across the QPC, whereas the bottom three images (Fig. 3, D to F) were taken at high voltage (3 mV). High voltage raises the energies of electrons flowing from the QPC: One would expect it to have the effect of thermally smearing out the coherent fringes. The fact that the  $\lambda_F/2$  fringes disappear with high effective electron temperature is additional confirmation that they are caused by coherent quantum interference. The angular envelope of electron flow remains unchanged at high voltage (Fig. 3, D to F). We will use these images of the envelope to analyze the angular contribution of electron flow from each transverse mode.

Figure 4, A to C, shows measured images of the angular pattern of electron flow from the first, second, and third transverse modes of the QPC. These images of flow from individual modes are obtained from images of

total electron flow (Fig. 3, D to F) by subtracting the flow pattern for a narrower QPC. For example, Fig. 4B (electron flow from only the second mode) was obtained by subtracting Fig. 3D (electron flow from the first mode) from Fig. 3E (electron flow from the first and second modes). Likewise, Fig. 4C (electron flow from just the third mode) was obtained by subtracting Fig. 3E (electron

flow from the first and second modes) from Fig. 3F (electron flow from the first, second, and third modes). One feature of these three images is that the number of lobes in the angular flow pattern equals the number of the point contact mode. This result makes intuitive sense because the same is true for the wavefunctions of electrons inside the point contact itself: Electronic wavefunctions pass-

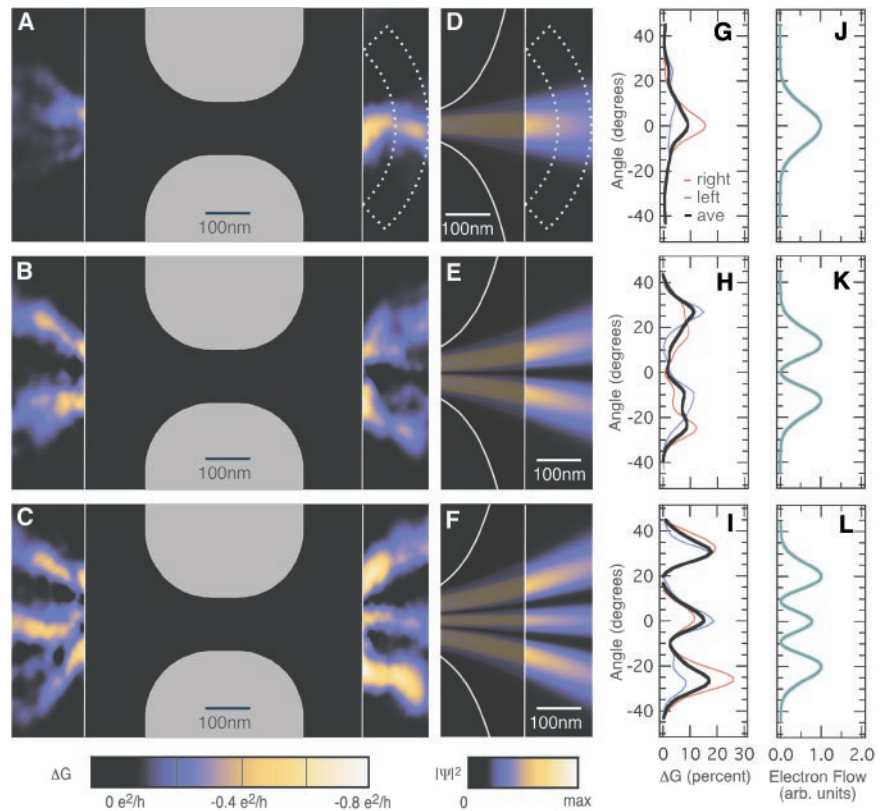
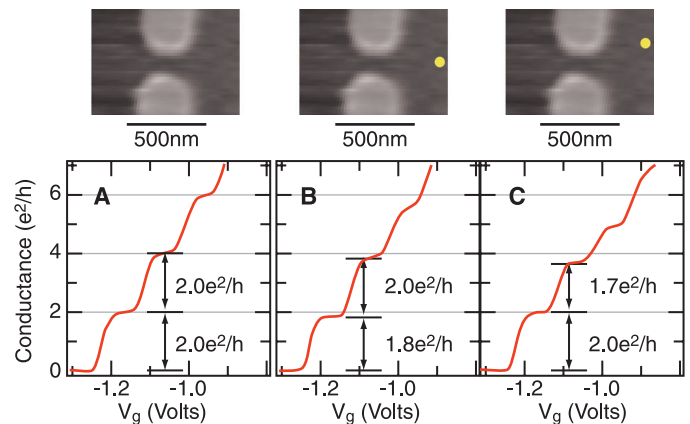


**Fig. 4.** (A to C) Angular pattern of electron flow of individual modes of the QPC, comparing experiment with theory [(A) first mode, (B) second mode, (C) third mode (see text)]. (D to F) Calculated wavefunction  $|\Psi|^2$  for electrons passing from (D) the first mode, (E) the second mode, and (F) the third mode of the QPC (the areas in each simulation corresponding to areas not scanned in the experiment are dimmed). (G to I) Measured angular distribution of electron flow from (G) the first mode, (H) the second mode, and (I) the third mode. (J to L) Angular distribution of the wavefunction  $|\Psi|^2$  from (J) the first mode, (K) the second mode, and (L) the third mode.

**Fig. 5.** The selective effect of the AFM tip on conductance plateaus of the QPC (the yellow circle indicates the position of the tip). (A) Conductance plateaus with no AFM tip. (B) Suppression of the first conductance plateau when the AFM tip is located directly in front of the QPC, blocking the electron flow from the first mode. (C) Suppression of the second conductance plateau when the tip is located  $15^\circ$  off the axis of the QPC, blocking electron flow from the second mode.



ing from the  $N$ th mode in a point contact have  $N$  maxima in  $|\Psi|^2$  (where  $\Psi$  is the wavefunction).

In the full quantum mechanical calculations of the pattern of electron flow from the lowest three modes of a QPC (Fig. 4, D to F), the color scale represents the wavefunction  $|\Psi|^2$  of electrons [Figs. 4D (first mode), 4E (second mode), and 4F (third mode)]. The wavefunction patterns agree well with images of electron flow; in both, the angular pattern of electrons flowing from the  $N$ th mode has  $N$  lobes. For these calculations, the transverse potential of the QPC was parabolic, with varying curvature to produce an electron gas channel approximating the lithographic shape of the gates; the white curves in Fig. 4, D to F, show where the potential crosses the Fermi energy. To ease comparison, areas not scanned in the experiment are dimmed in the simulation.

Figure 4, G to I, plots the angular distribution of measured electron flow in Fig. 4, A to C. The circular slice used to determine the distribution is shown in Fig. 4A. Figure 4, J to L, plots the angular distribution of electron wavefunctions  $|\Psi|^2$  from Fig. 4, D to F, taken using a circular slice shown in Fig. 4D. Comparison shows a high degree of agreement between theory and experiment. The measured angular dependencies of images and theory have the same modal structure ( $N$  lobes for the  $N$ th transverse mode), and they agree quite well in shape.

The height of the  $N$ th conductance plateau is changed when the AFM tip is held at a fixed position above the electron flow pattern from the  $N$ th mode of the QPC (Fig. 5). When no tip is present (Fig. 5A), each transverse mode contributes  $2 e^2/h$  of conductance. When the tip is placed directly in front of the QPC (Fig. 5B), it backscatters electrons from the first mode without affecting electrons from the second (Fig. 4D). This reduces the entire first plateau to  $1.8 e^2/h$  without changing the spacing between the first and second plateaus. When the tip is placed off-axis as in Fig. 5C, it backscatters electrons from the second mode without affecting electrons from the first (Fig. 4E). This reduces the spacing between the first and second plateaus to  $1.7 e^2/h$  without affecting the height of the first plateau.

We have presented spatial images that show the coherent flow of electron waves through semiconductor nanostructures. The observation of the expected angular structure of electron flow from the first, second, and third modes of a QPC, as well as the clear appearance of fringes separated by half the Fermi wavelength  $\lambda_F/2$ , are strong confirmations of this imaging technique. These results are a confirmation of the power that SPMs have for imaging the flow of electron waves through mesoscopic semiconductor devices. The ability to image elec-

tron wave flow inside GaAs/AlGaAs heterostructures makes possible future experiments, including spatial investigations of quantum coherence, universal conductance fluctuations, and weak localization.

References and Notes

- M. F. Crommie, C. P. Lutz, D. M. Eigler, *Science* **262**, 218 (1993).
- E. J. Heller, M. F. Crommie, C. P. Lutz, D. M. Eigler, *Nature* **369**, 464 (1994).
- H. C. Manoharan, C. P. Lutz, D. M. Eigler, *Nature* **403**, 512 (2000).
- M. A. Eriksson *et al.*, *Appl. Phys. Lett.* **69**, 671 (1996).
- R. Crook, C. G. Smith, C. H. W. Barnes, M. Y. Simmons, D. A. Ritchie, *J. Phys. Cond. Mat.* **12**, L167 (2000).
- M. J. Yoo *et al.*, *Science* **276**, 579 (1997).
- K. L. McCormick *et al.*, *Phys. Rev. B* **59**, 4654 (1999).
- N. B. Zhitenev *et al.*, *Nature* **404**, 473 (2000).
- G. Finkelstein, P. I. Glicofridis, R. C. Ashoori, M. Shayegan, *Science* **289**, 90 (2000).
- L. Gurevich, L. Canali, L. P. Kouwenhoven, *Appl. Phys. Lett.* **76**, 384 (2000).
- B. J. van Wees *et al.*, *Phys. Rev. Lett.* **60**, 848 (1988).
- D. A. Wharam *et al.*, *J. Phys. C Solid State Phys.* **21**, 209 (1988).
- Reviewed in C. W. J. Beenakker and H. van Houten, *Solid State Phys.* **44**, 1 (1991).
- L. W. Molenkamp *et al.*, *Phys. Rev. B* **41**, 1274 (1990).
- K. L. Shepard, M. L. Roukes, B. P. van der Gaag, *Phys. Rev. Lett.* **68**, 2660 (1992).
- The tips used were piezoresistive cantilevers from ThermoMicroscopes, Sunnyvale, CA; see also M. Tortorese, R. C. Barret, C. F. Quate, *Appl. Phys. Lett.* **62**, 834 (1993).
- D. P. DiVincenzo, in *Mesoscopic Electron Transport*, L. L. Sohn, L. P. Kouwenhoven, G. Schön, Eds. (Kluwer Academic, Boston, MA, 1997), pp. 657–677.
- The average spacing of these fringes is  $22 \pm 2$  nm, and the expected spacing from the sheet density is  $\lambda_F/2 = 19$  nm. The difference can be attributed to a lower sheet density in the area of the device as compared with the bulk, because of the negatively charged gates and AFM tip.
- B. L. Altshuler, A. G. Aronov, D. E. Khmel'nitsky, *J. Phys. C* **15**, 7367 (1982).
- Supported in part at Harvard University by Office of Naval Research/Augmentation Awards for Science and Engineering Research Training (ONR/AASERT) grant N00014-97-1-0770, by ONR grant N00014-95-1-0104, and by NSF under grant NSF-CHE9610501 and Harvard's Materials Research Science and Engineering Center grant DMR-98-09363. M.A.T. and S.E.J.S. were supported by NSF graduate fellowships. This work was supported at the University of California, Santa Barbara, by NSF Science and Technology Center QUEST.

1 June 2000; accepted 22 August 2000

## Technique for Enhanced Rare Earth Separation

Tetsuya Uda,<sup>1\*</sup> K. Thomas Jacob,<sup>2</sup> Masahiro Hirasawa<sup>1</sup>

A process is demonstrated for the efficient separation of rare earth elements, using a combination of selective reduction and vacuum distillation of halides. The large differences in the redox chemistry of the rare earth elements and in the vapor pressures of rare earth di- and trihalides are exploited for separation. Experimental proof of concept is provided for the binary systems praseodymium-neodymium and neodymium-samarium. This process enhances the separation factor for the isolation of samarium and neodymium from their mixture by more than an order of magnitude.

Rare earth elements and compounds find application in many advanced materials of current interest such as high-performance magnets, fluorescent materials, chemical sensors, high-temperature superconductors, magneto-optical disks, and nickel-metal hydride batteries. Powerful rare earth permanent magnets such as  $\text{Nd}_2\text{Fe}_{14}\text{B}$  and  $\text{SmCo}_5/\text{Sm}_2\text{Co}_{17}$  have revolutionized technology, allowing miniaturization of devices such as the hard disk drive and compact disc player. However, the production cost of rare earth permanent magnets is very high, because of the high cost of extracting pure Sm or Nd metal used in their manufacture. The separation of individ-

ual rare earth elements is a difficult process involving solvent extraction or ion exchange (1–3). Because the chemical properties of rare earth ions in aqueous solution exhibit only incremental variation with atomic number, solvent extraction must be repeated many times. The ion exchange process is not suitable for industrial production because of the very long periods (greater than 10 days) required to accomplish significant separation. A dry process was recently developed for the separation of rare earth elements (4, 5) using chemical vapor transport mediated by a gaseous complex such as  $\text{LnAlCl}_3$  (Ln: lanthanoid). However, the separation efficiency with the dry process for adjacent elements in the periodic table was lower than that obtained in the conventional solvent extraction process (6). We present a more efficient separation method, which combines selective reduction with vacuum distillation.

Although rare earth elements are usually present as trivalent ions in their compounds,

<sup>1</sup>Research Center for Metallurgical Process Engineering, Institute for Advanced Materials Processing, Tohoku University, Sendai 980-8577, Japan. <sup>2</sup>Department of Metallurgy, Indian Institute of Science, Bangalore 560 012, India.

\*To whom correspondence should be addressed. E-mail: uda@iamp.tohoku.ac.jp